Lectures in Paleomagnetism, 2005
by Lisa Tauxe

Citation:
http://earthref.org/MAGIC/books/Tauxe/2005/

June 8, 2005

Chapter 13

Paleomagnetic tensors

Suggested Reading

For background:
Part II: Means (1976)
Tarling and Hrouda (1993)
Chapter 2: Collinson (1983)
To learn more:
Chapters 5 and 6: Tauxe (1998)

13.1 Introduction

In the previous several lectures we have been concerned with magnetic vectors. Higher dimensional magnetic tensors are also tremendously useful in geological studies and have found wide use in studies involving sedimentary, igneous and metamorphic rocks. Such data have applications in determining such varied parameters as paleocurrent directions, degree of paleosol maturity, directions of magma injection, tectonic strain, etc. The most frequently used magnetic tensors are the anisotropy of magnetic susceptibility (AMS) and the anisotropy of anhysteretic remanence (AARM) tensors, although TRM, DRM and IRM anisotropy are also measured from time to time. We will begin by describing the measurement of magnetic susceptibility and how the AMS tensor is determined. Then we will extend the discussion to the anisotropy of remanences.

13.2 Measurement of magnetic susceptibility

The concept of magnetic susceptibility was first introduced in Lecture 1. It is usually taken as the ratio of the induced magnetization to an inducing magnetic field or M_I/H. In practice, many laboratories use equipment that works on the principle illlustrated in Figure 13.1 whereby an alternating current is driven through the coil on the right inducing a current in the coil on the left. This alternating current generates a small alternating field (generally less than 1 mT) along the axis of the coil. When a sample is placed in the coil, the alternating current induces an alternating magnetic field in the sample. This causes an offset in the alternating current in the coil on the right which is proportional to the induced magnetization. After calibration, this offset can then be cast in terms of magnetic susceptibility. If the sample is placed in the solinoid in different orientations (e.g., those in Figure 13.1d), the anisotropy of the magnetic susceptibility can be determined.

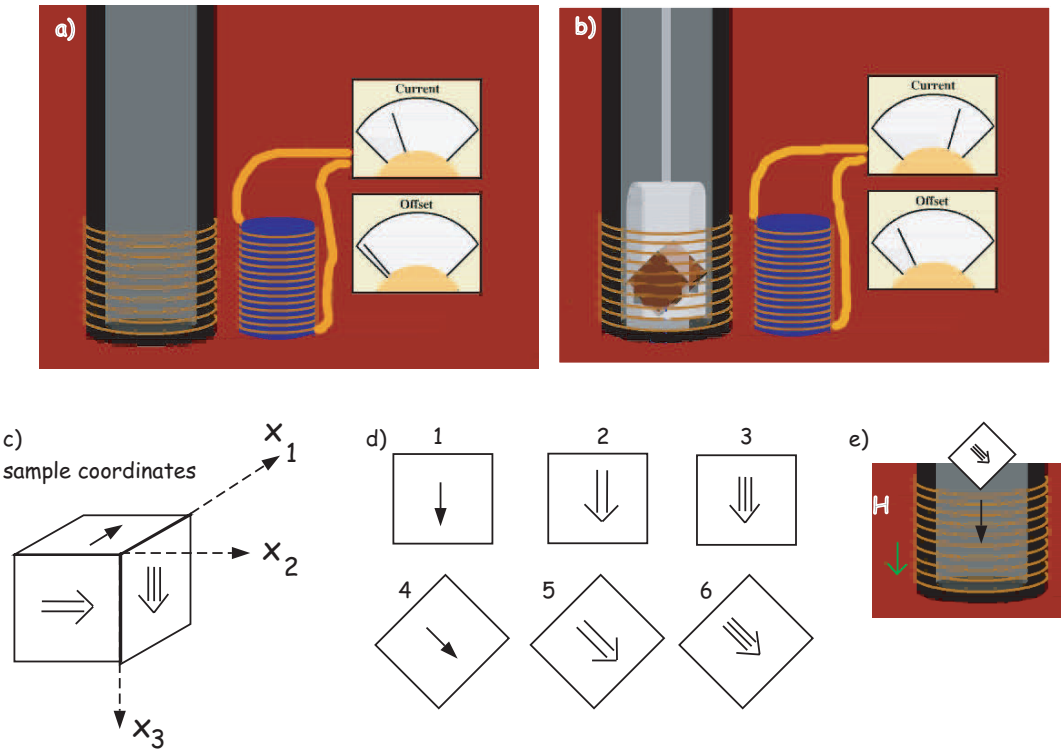

Figure 13.1: Measuring magnetic susceptibility. a) An alternating current applied in the coil on the right induces a current in the left-hand coil. This induces a magnetization in the sample shown in b), which in turn offsets the current in the coil to the right. The offset is proportional to the magnetic susceptibility of the sample. [Figure modified from Genevieve Tauxe, http://magician.ucsd.edu/Lab_tour/movs/isosuscp.mov.] c) Definition of sample coordinates. d) Scheme for measuring six elements of **K**. d) The sample is placed in the different orientations in the coil as in e) with alternating field **H**.

Before we launch into a detailed discussion of AMS data it is worth thinking briefly about what controls magnetic susceptibility and what the data might mean. At an atomic level, magnetic susceptibility results from the response of electronic orbits and/or unpaired spins to an applied field (Lecture 3). The diamagnetic response (orbits) is extremely weak and unless a specimen is nearly pure carbonate or quartz, it can be neglected. The paramagnetic response of, say, biotite, is much stronger, but if there is any appreciable ferromagnetic material in the specimen, the response will be dominated by that.

In highly magnetic minerals such as magnetite, the susceptibility is dominated by the shape anisotropy. For a uniformly magnetized particle (e.g., small SD magnetite), the maximum susceptibility is at a high angle to the easy axis, because the moments are already at saturation along the easy direction. So we have the somewhat paradoxical result that uniformly magnetized particles have maximum susceptibilities along the short axis of elongate grains. For vortex remanent state, or multi-domain particles and perhaps for strongly flowered grains, this would not be the case and the maximum susceptibility is along the particle length. Another perhaps non-intuitive behavior is for superparamagnetic particles whose response is quite large (some 25 times larger than a sin-

gle domain particle of the same size!). Chains of particles may also have non-intuitively obvious magnetic responses because of interparticle interaction.

Ferromagnetic phases can occur as discrete grains in rocks or as inclusions within other mineral phases. Often the magnetic phases in silicate hosts like plagioclase are crystallographically aligned. The AMS response can therefore be controlled by the alignment of the host minerals, by the alignment of interacting chains of magnetic particles or by the alignment of the discrete magnetic grains in the rock. Therefore care must be exercised in the interpretation of AMS results.

The relationship between a small applied magnetic field vector **H** and the induced magnetization vector **M** until now has been taken as a scalar. However, if the magnetic response of the specimen depends on the orientation of the applied field (i.e., it is anisotropic) it can often be approximated by a small set of linear equations. Components of the induced magnetization in a given coordinate system ($\mathbf{M}_i$) whose axes are denoted by $\mathbf{X}_1, \mathbf{X}_2$, and $\mathbf{X}_3$ (see Figure 13.1c) are related to the components of the applied field along the sample axes $\mathbf{H}_i$ (see Lecture 2) by the following linear equations:

$$\begin{aligned} M_1 &= \chi_{11}H_1 + \chi_{12}H_2 + \chi_{13}H_3 \\ M_2 &= \chi_{21}H_1 + \chi_{22}H_2 + \chi_{23}H_3 \\ M_3 &= \chi_{31}H_1 + \chi_{32}H_2 + \chi_{33}H_3, \end{aligned} \tag{13.1}$$

where χ_{ij} are coefficients of magnetic susceptibility.

13.3 Treatment of anisotropy data

The linear relationship between the two vectors can be cast as a second-order tensor. The coefficients χ_{ij} are the elements of a second-order, symmetric tensor, known as the *anisotropy of magnetic susceptibility (AMS) tensor* χ. The set of Equations 13.1 can be rewritten in subscript notation as:

$$M_i = \chi_{ij}H_j. \tag{13.2}$$

Because $\chi_{ij} = \chi_{ji}$, the susceptibility tensor χ defines a symmetric, second-order tensor that has 6 independent matrix elements. For convenience we define a related column matrix **s** having six elements that are related to the elements of χ by:

$$\begin{aligned} s_1 &= \chi_{11} \\ s_2 &= \chi_{22} \\ s_3 &= \chi_{33} \\ s_4 &= \chi_{12} = \chi_{21} \\ s_5 &= \chi_{23} = \chi_{32} \\ s_6 &= \chi_{13} = \chi_{31}. \end{aligned} \tag{13.3}$$

In practice, only s_1, s_2, and s_3 can be measured directly, the terms s_4 to s_6 are only indirectly determined. In the simplest experiment,, there are six measured values of susceptibility K_i. These are determined in six sample positions, for example, as shown in Figure 13.1d. Measurement in position 1 gives $K_1 = s_1$. Similarly, in position 2, we measure $K_2 = s_2$, and in position 3, we get $K_3 = s_3$. But, $K_4 = \frac{1}{2}(s_1 + s_2) + s_4$, $K_5 = \frac{1}{2}(s_2 + s_3) + s_5$, and $K_6 = \frac{1}{2}(s_1 + s_3) + s_6$. From this we see that the elements of **s** are related to the matrix of measurements **K** in subscript notation by:

$$K_i = A_{ij}s_j, \tag{13.4}$$

where **A** depends on the experimental design and is called the *design matrix*. The measurement scheme shown in Figure 13.1, has the design matrix:

$$\mathbf{A} = \begin{pmatrix} 1 & 0 & 0 & 0 & 0 & 0 \\ 0 & 1 & 0 & 0 & 0 & 0 \\ 0 & 0 & 1 & 0 & 0 & 0 \\ .5 & .5 & 0 & 1 & 0 & 0 \\ 0 & .5 & .5 & 0 & 1 & 0 \\ .5 & 0 & .5 & 0 & 0 & 1 \end{pmatrix}. \tag{13.5}$$

Although there are six measurements and six unknowns, the elements of **s** are overdetermined, because the diagonal measurements depend on three parameters. In order to calculate the best-fit values $\bar{\mathbf{s}}$ for **s**, we can use linear algebra:

$$\bar{\mathbf{s}} = (\mathbf{A}^T\mathbf{A})^{-1}\mathbf{A}^T\mathbf{K} \quad \text{or} \quad \bar{\mathbf{s}} = \mathbf{B}\mathbf{K}, \tag{13.6}$$

where $\mathbf{A}^T$ is the transpose of **A**. The elements of **B** for the scheme shown in Figure 13.1 are readily determined as:

$$\mathbf{B} = \begin{pmatrix} 1 & 0 & 0 & 0 & 0 & 0 \\ 0 & 1 & 0 & 0 & 0 & 0 \\ 0 & 0 & 1 & 0 & 0 & 0 \\ -.5 & -.5 & 0 & 1 & 0 & 0 \\ 0 & -.5 & -.5 & 0 & 1 & 0 \\ -.5 & 0 & -.5 & 0 & 0 & 1 \end{pmatrix}. \tag{13.7}$$

In the special case in which **A** is a square matrix (as in Equation 13.5), $(\mathbf{A}^T\mathbf{A})^{-1}\mathbf{A}^T$ reduces to $\mathbf{A}^{-1}$ (i.e. $\mathbf{B} = \mathbf{A}^{-1}$).

There exists one coordinate system **V** (whose axes are the eigenvectors of χ: $\mathbf{V}_1$, $\mathbf{V}_2$, $\mathbf{V}_3$) in which the off-axis terms of χ are zero (see Appendix C of Lecture 9). In this special coordinate system:

$$\begin{aligned} M_1 &= s_1 H_1 = \chi_{11} H_1 \propto \tau_1 H_1 \\ M_2 &= s_2 H_2 = \chi_{22} H_1 \propto \tau_2 H_2 \\ M_3 &= s_3 H_3 = \chi_{33} H_3 \propto \tau_3 H_3. \end{aligned} \tag{13.8}$$

The eigenvalues τ_1, τ_2 and τ_3 correspond to the maximum, intermediate, and minimum susceptibility, respectively. These are the susceptibilities along the principal, major and minor eigenvectors $\mathbf{V}_1$, $\mathbf{V}_2$, and $\mathbf{V}_3$, respectively. Scaling χ by its trace yields values for τ that sum to unity. [Note that $\mathbf{V}_1, \mathbf{V}_2$ and $\mathbf{V}_3$ are sometimes referred to as K_{max}, K_{int}, and K_{min}, respectively in the literature.]

When the coordinate system of the susceptibility data is defined by the eigenvectors, then the components of magnetization M_i satisfy the following:

$$\frac{M_1^2}{\tau_1^2} + \frac{M_2^2}{\tau_2^2} + \frac{M_3^2}{\tau_3^2} = 1. \tag{13.9}$$

The surface described by Equation 13.9 illustrated in Figure 13.2b traces an ellipsoid termed the *magnitude ellipsoid* by Nye (1957) whose semi-axes are directed along **V** and have lengths that are proportional to the τ_i. We will refer to this ellipsoid in the following as the anisotropy of magnetic susceptibilty (AMS) ellipsoid. Because it is possible to have negative eigenvalues making the magnitude ellipsoid difficult to visualize, some workers prefer the representation quadric, which

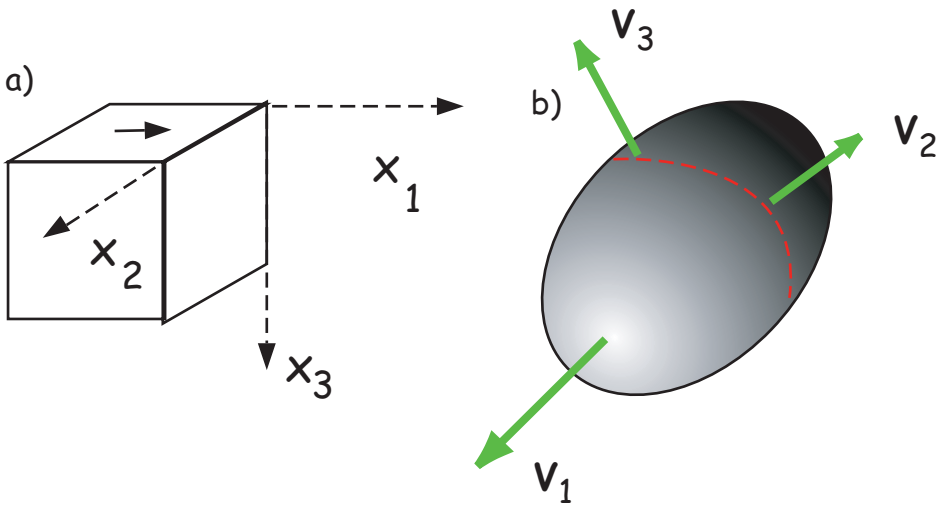

Figure 13.2: a) Arbitrary coordinate system of a specimen. b) The magnitude ellipsoid of of the AMS. Its coordinate system is defined by the eigenvectors $\mathbf{V}_1$ and $\mathbf{V}_2$. The lengths along the eigenvectors of the ellipsoid surface are related to the eigenvalues (see text).

has a less direct relationship to the eigenvalues. In the case of negative eigenvalues (say for a carbonate dominated system), it is also possible to simply offset the eigenvalues by some DC offset to ensure positivity.

Many publications list AMS data in terms of the eigenvalues and eigenvectors, collectively referred to as eigenparameters so it is handy to have a way to transform eigenparameters back into matrix elements. This can be done using tricks from linear algebra:

$$\chi = \mathbf{V}\tau\mathbf{V}^T, \tag{13.10}$$

where $\mathbf{V}^T$ is the transpose of $\mathbf{V}$. [Note that several (maybe even three) decimal places are required to do this inversion in a satisfactory fashion, yet almost no one reports to this degree of precision and the tensor elements you get back out may be very different than those that went in if there is insufficient precision.]

The eigenparameters of the susceptibility tensor are related to the statistical alignment of dia-, para-, and/or ferromagnetic phases within the rock and the AMS ellipsoid can be used to describe the magnetic fabric of the rock. Much of the interpretation of AMS data in the literature revolves around an assessment of directions of principal axes and relative magnitudes of the eigenvalues.

There is a bewildering variety of conventions for describing the relationships among the three eigenvalues (see, Table 13.1 for a partial list). A practical initial classification scheme can be made with the following rules: when ($\tau_1 \simeq \tau_2 \simeq \tau_3$), the shape is a sphere; when ($\tau_1 \simeq \tau_2 > \tau_3$), it is oblate. The shape is prolate when ($\tau_1 > \tau_2 \simeq \tau_3$), and, finally, the anisotropy ellipsoid is triaxial when ($\tau_1 > \tau_2 > \tau_3$). Because there are nearly always three distinct values of τ, it is a statistical problem to decide whether the eigenvalues from a given data set are significantly different from one another.

Making only six measurements allows calculation of the eigenparameters, but gives no constraints for their uncertainties. We would like to ask questions such as the following:

1) Is a particular axis parallel to some direction? Is $\mathbf{V}_3$ vertical as might be expected for a primary sedimentary fabric? Is $\mathbf{V}_1$ parallel to some lineation such as elongated vesicles in volcanic dikes, or deformed ooids in strained rocks?

2) Are two sets of eigenvectors distinct? Are data from two sides of a dike margin imbricated, allowing interpretation of flow direction? Has progressive strain rotated the rock fabrics?

3) What is the shape of the AMS ellipsoid? Are the eigenvalues distinct? Is the fabric oblate, as for consolidated, undeformed sedimentary rocks? Does the shape change as a result of progressive deformation in metamorphic rocks?

In order to address questions such as these, we need some sort of confidence intervals for the eigenparameters; hence we need to make multiple measurements and we need a means of translating the measurements into uncertainties in AMS data. The principles of error analysis for anisotropy measurements were originally laid out by Hext (1963), and were later fleshed out by Jelinek (1976, 1978). These are analytical approaches. Constable and Tauxe (1990) took an entirely different approach using a bootstrap. We will begin with the Hext (1963) method which serves as the foundation for all modern AMS statistical analysis.

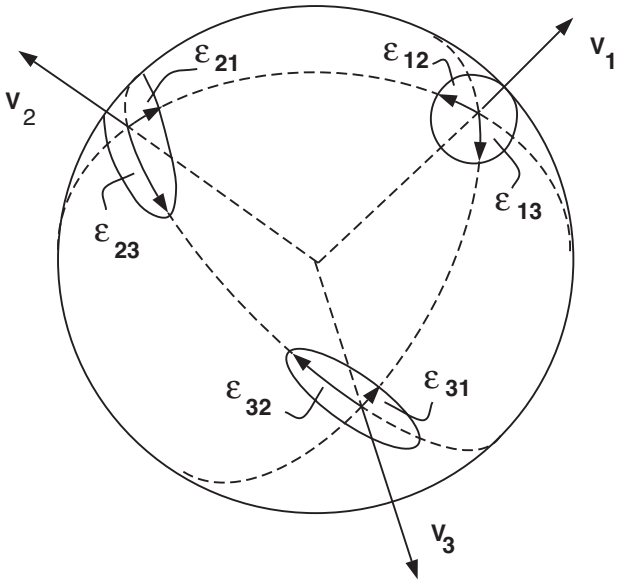

Figure 13.3: Relationship of the uncertainty ellipses (calculated by Hext statistics for AMS data) to the principal axes. The major and minor semi-axes of the uncertainty ellipses are oriented along the axes defined by the eigenvectors.

13.4 Hext Statistics

According to Hext (1963), each measurement K_i has an unknown measurement "error":

$$K_i = A_{ij} s_j + \delta_i. \tag{13.11}$$

The residual sum of squares S_o is:

$$S_o = \sum_i \delta_i^2, \tag{13.12}$$

and the estimated variance is:

$$\sigma^2 = S_o/n_f. \tag{13.13}$$

n_f is the number of degrees of freedom, given by $N_{meas} - 6$ where N_{meas} is the number of measurements and six is the number of measurements required to determine the susceptibility tensor.

There are many measurement schemes in common usage with as few as six (for which of course σ^2 is undefined) and as many as several hundred. The scheme of Jelinek (1976), has the number of measurements $N_{meas} = 15$, and is described in detail in the Appendix as it is currently perhaps the most widely used.

Each measurement system has an associated design matrix from which the **B** matrix can be determined. That for the 15 measurement scheme can be found in the Appendix. Once the **B** matrix is set up, we can calculate the best-fit values for **s**:

$$\bar{s}_i = B_{ij} K_j. \tag{13.14}$$

The best-fit values for **K** ($\bar{\mathbf{K}}$) can then be calculated by substituting the right **A** matrix (see e.g., Appendix):

$$\bar{K}_i = A_{ij} \bar{s}_j.$$

Now we can calculate the δ_i by:

$$\delta_i = K_i - \bar{K}_i, \tag{13.15}$$

and S_o is given by Equation 13.12.

Assuming that the uncertainties in **K** (the δ_i) have zero mean, and that they are uncorrelated, normally distributed, and small (so that the products of uncertainties can be neglected), Hext (1963) proposed that approximate 95% confidence ellipses for the eigenvectors (see Figure 13.3) can be calculated as described in the Appendix.

We turn now to the problem of calculating confidence intervals for the eigenvalues. In practice, there will almost always be three distinct values of τ returned from an eigenvalue calculation. But, when are these values statistically distinct? First, one might ask if the ellipsoid is significantly different from a sphere. Hext statistics allows calculation of F statistics and comparison with values in F tables (Appendix to Lecture 11); in this way one can test if the data are isotropic (F) ($\tau_1 = \tau_2 = \tau_3$), if $\tau_1 = \tau_2$ (F_{12}), or if $\tau_2 = \tau_3$ (F_{23}). Calculation of the F statistics is given in the Appendix. F values below the critical values do not allow rejection of the hypothesis of isotropy or rotational symmetry, respectively.

13.5 Anisotropy of magnetic remanence

Magnetic susceptibility is in many ways like color in that many things contribute and often it is as difficult to interpret. Magnetic remanence is a much more targeted parameter because only ferromagnetic particles contribute to it and certain remanences are sensitive to only particular minerals or grain sizes. Hence anisotropy of magnetic remanence can be a more subtle instrument than AMS. Furthermore, certain applications such as paleointensity, paleodirectional determinations or correction of inclination error may require the anisotropy of the TRM or DRM to be taken into

account. For example, paleointensity on pot sherds or other anisotropic specimens must be corrected for specimen's anisotropy (e.g., Aitken et al. 1981) and the inclination "error" of DRM (see Lecture 5) can be corrected using information from ARM anisotropy (e.g., Jackson et al. 1991).

ARM is often considered analogous to TRM. Its acquisition is mathematically identical, relying instead on variations in applied field as opposed to temperature as a blocking mechanism (see Lecture 5). It is far more convenient to give a sample an ARM than a TRM in the laboratory, so ARM and ARM anisotropy are frequently substituted for the analogous TRM. Of course, the two are NOT identical and proper care should be taken to ensure that the appropriate remanence is used for the particular purpose. Nonetheless, anisotropy of ARM (AARM) is a useful measurement and we describe first how AARM is determined in the SIO laboratory. There are slight experimental differences between AARM and ATRM which will be noted.

13.5.1 Anisotropy of ARM and TRM

Prior to acquisition of the laboratory remanence, the specimen should be in a fully demagnetized state which is measured as a baseline. Then one applies an ARM in at least three directions (say positions 1, 2 and 3 in Figure 13.1d). Generally, from six to 15 orientations for the ARM are used to get a reasonable estimate of the uncertainties. Between each position, the specimen should be demagnetized along the axis of the subsequent ARM. This measurement is substracted from the subsequent ARM by vector subtraction. Each ARM step (after subtraction of the baseline) gives three orthogonal remanence components (K^R_{ij}). Please note that it is possible to give ARMs in the presence of different AF fields from very high (presumably a total ARM) to lower (giving a partial ARM of pARM). The DC field is also variable, but should be in the region where the (p)ARM is linearly related to the DC field.

The main difference between AARM and ATRM in procedure is that the demagnetization step is not required in TRM. Instead, the sample is simply placed in each direction without the intervening baseline step.

The equation for anisotropy of magnetic remanence that is analogous to Equation 13.1 is $M_i = \chi^R_{ij} H_j$ where χ^R are the coefficients for the remanent anisotropy. These can be reduced to the elements of $\mathbf{s}$ by multiplying by the appropriate $\mathbf{B}$ matrix, depending on the number and orientation of positions used in the experiment. Because each measurement yields information along three axes, the design matrix has three times as many elements as for the AMS experiment with the same number of measurements. For example, for a six position experiment, the design matrix is 18 x 6 instead of 6x6. After determining $\mathbf{s}$, the other Hext parameters can be determined as before, using $n_f = 3N_{meas} - 6$.

13.5.2 Anisotropy of DRM

We learned in Lecture 5 that the inclination of DRM is often too shallow and that it follows the tangent function:

$$\tan I_o = f \tan I_f, \tag{13.16}$$

where I_o and I_f are the observed DRM inclination and the applied field inclination respectively (King, 1955). The parameter f is the "flattening factor".

Jackson et al. (1991) restate the relationship of the DRM (M_d) to the applied field $\mathbf{H}$ as:

$$M_d = \mathbf{k_d H}$$

where $\mathbf{k_d}$ is the DRM tensor. The eigenvalues of the $\mathbf{k_d}$ matrix are here referred to as κ_{d_i} where κ_{d_1} is here taken as the largest for consistency with the rest of these Lecture Notes. Jackson et al. (1991) demonstrated that the flattening factor f is equivalent to the ratio $\kappa_{d_3}/\kappa_{d_1}$. Therefore the trick to correcting flattened inclinations is to estimate $\mathbf{k_d}$.

There could be several ways of estimating the DRM tensor in the lab: directly, by redeposition or indirectly, by measuring the anisotropy of a proxy remanence (say ARM). Redeposition is in practice quite problematic because it is rarely possible to recreate the original depositional conditions of grain size, water chemistry, particle flux, turbulence and so on that might play a role in determining the anisotropy tensor. The proxy approach is straightforward in the lab, but difficult to tie directly to the DRM anisotropy. What is required is a laboratory remanence that closely targets the same spectrum of coercivities as that carrying the DRM. By AF demagnetizing the NRM and an ARM or a pARM it can be shown that the (p)ARM often satisfies this requirement (see e.g., Levi and Banerjee 1976). From this, Jackson et al. (1991) argue that the ARM tensor is the best proxy remanence for the DRM.

The relationship between the ARM and DRM anisotropy tensors is not straightforward. Jackson et al. (1991) consider the complexity of the processes that align and misalign particle long-axes, including the external magnetic field, gravitational, compactional, electrostatic, surface tension and Van der Waal's forces. The result of all of these is only a slight net alignment (as discussed in Lecture 5). Under certain circumstances including post-depositional compaction and syn-depositional effect of elongate particles landing on the sediment/water interface, there can be preferential alignment in the horizontal plane leading to inclination shallowing.

In order to tie the AARM tensor to the DRM anisotropy tensor, we need to determine the orientations of the particle long axes as well as the effects of individual particle anisotropies. This latter results from the fact that individual particles are not ordinarily at saturation being generally (except for very small grains or grains of low magnetization materials) non-uniformly magnetized themselves (e.g., vortex remanence state). The rationale is that because AARM reflects the variations in the capacity for carrying remanence in the detrital particles, that AARM can be used to determine the anisotropy of DRM, if the ARM anisotropy of the detrital particles themselves can be determined. The details of how this are done in practice is summarized in the Appendix.

13.6 When are data suitable for Hext statistics?

The assumptions for using the techniques outlined in the foregoing are that the uncertainties in the measurements have zero mean, are normally distributed, and are small. While measurement error using modern equipment is likely to be quite small, data from a collection of samples often do not conform to these restrictive assumptions. In particular, the δ values are often large.

Constable and Tauxe (1990) showed that, in general, δs from AMS data calculated for multiple samples (that must be normalized by their trace) will not generally be normally distributed. Hence, data incorporating multiple samples are often not amenable to Hext statistics. A bootstrap for paleomagnetic tensors is described in the next section. In the rest of the lecture, we will continue our discussion of anistropy and paleomagnetic tensors with a brief discussion of remanence anisotropy.

13.7 Bootstrap confidence ellipses

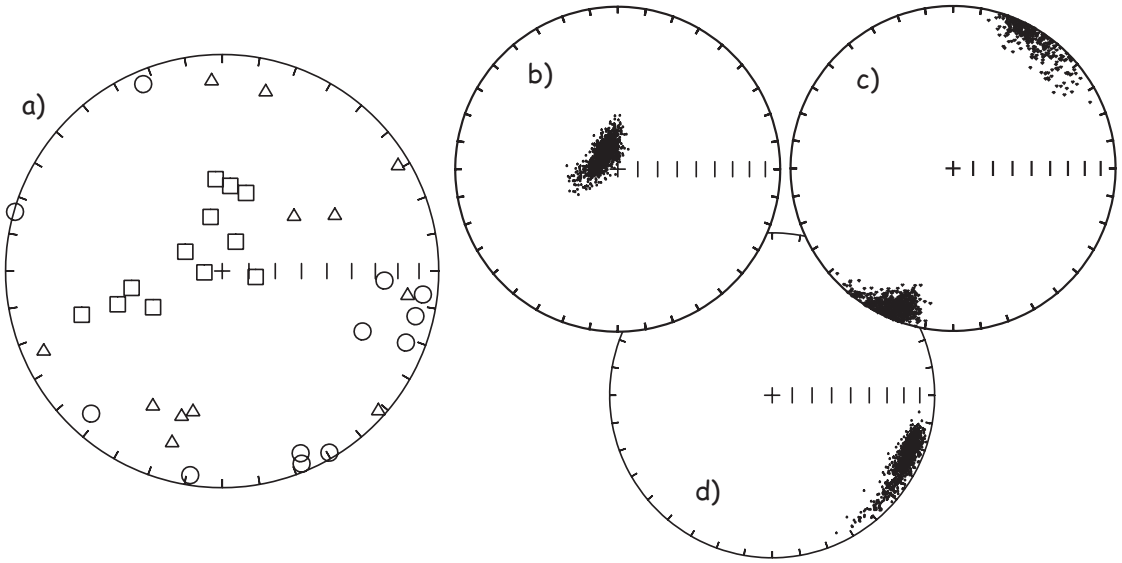

Figure 13.4: a) Lower hemisphere projection of directions of $\mathbf{V}_1$ (squares), $\mathbf{V}_2$ (triangles), and $\mathbf{V}_3$ (circles) from the margin of a volcanic dike in the Troodos Ophiolite. b) Equal area projection of principal eigenvectors ($\mathbf{V}_1$) of 500 para-data sets drawn from the data in a). c) Same as b) for the major eigenvectors ($\mathbf{V}_2$). d) Same as b) for the minor eigenvectors ($\mathbf{V}_3$).

The eigenvector data in Figure 13.4a were obtained by analyzing numerous individually oriented samples from one of the quenched margins of a dike in the Troodos Ophiolite on Cyprus. We plot the eigenvectors on an equal area net using the lower hemisphere projection and follow the convention that the $\mathbf{V}_1$s are squares, $\mathbf{V}_2$s are triangles, and $\mathbf{V}_3$s are circles. The data are rather typical for those obtained from a single homogeneous body of rock in that the δ distributions that are neither normally distributed, nor small.

Constable and Tauxe (1990) developed a bootstrap for anisotropy data which is similar to that introduced in Lecture 12 for vectors. As in Lecture 12, we first take a number of randomly selected para-data sets of the data from those shown in Figure 13.4a. The eigenparameters of the bootstrapped average $\bar{s}$ matrices are then calculated. Such bootstrapped eigenvectors are shown in the equal area projections in Figure 13.4(b-d).

A non-parametric confidence region for the bootstrapped distributions shown in Figure 13.4b-d could be drawn as a contour line enclosing 95% of the bootstrapped eigenvectors. Because it is often useful to characterize the average uncertainties with a few parameters (for example, to put them in a data table), we can proceed as with the unit vectors and assume some sort of distribution for the eigenvectors, for example, the Kent distribution from Lecture 12). However, for most of the questions outlined at the beginning of the lecture, it is preferrable to assess directly the 95% confidence bounds on the parameter of interest.

By analogy with the bootstrap for unit vectors and the fold test, we can also perform parametric bootstraps. There are two flavors of these. The first flavor, the *sample parametric bootstrap*, proceeds as follows: After randomly selecting a particular sample for inclusion, each element of $\mathbf{s}$ is replaced by a simulated element drawn from a normal distribution having the σ as calculated for

the sample data. This Monte Carlo type simulation assumes that the measurement uncertainties are normally distributed, which is likely to be the case. If instrument noise is significant, then the sample parametric bootstrap is an important tool.

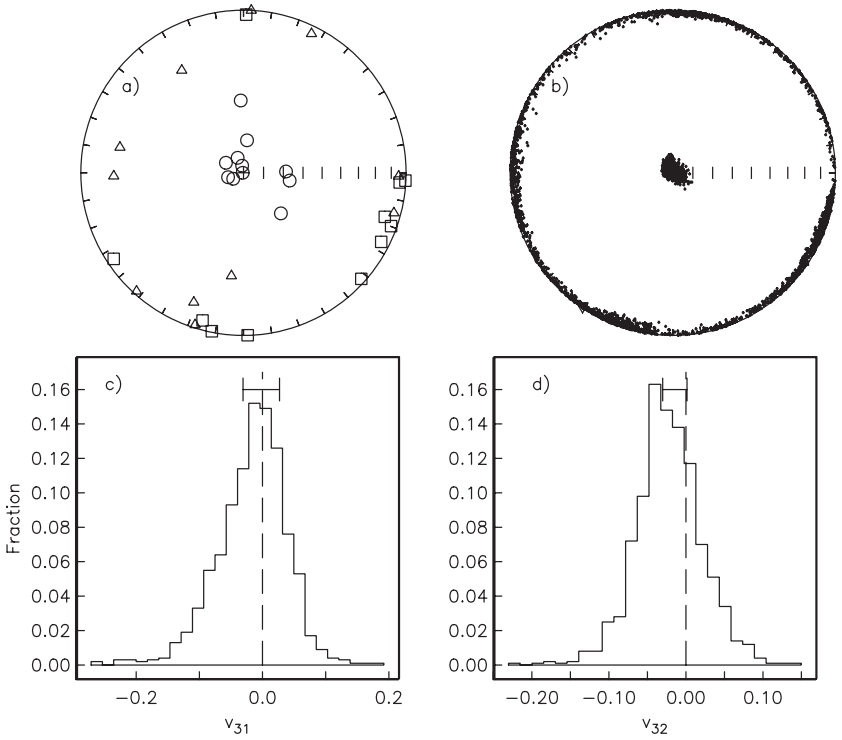

Figure 13.5: a) AMS data from Cretaceous carbonate limestones in Italy (the Scaglia Bianca Formation) in tilt adjusted coordinates. a) Lower hemisphere projections of the principal $\mathbf{V}_1$ (squares), major $\mathbf{V}_2$ (triangles), and minor $\mathbf{V}_3$ (circles) eigenvectors. b) Bootstrapped eigenvectors from para-data sets of the data in a). c) Histogram of the v_{31} components of $\mathbf{V}_3$ from b) with bounds containing 95% of the components. The zero value expected from a vertical direction is shown as a dashed line. d) same as c) but for the v_{32} component. Since both v_{31} and v_{32} are indistinguishable from zero, $\mathbf{V}_3$ is vertical at the 95% level of confidence.

Because the δ_i data from homogeneous rock bodies are often normally distributed, we can also perform a parametric bootstrap at the level of the site (the *site parametric bootstrap*). This is done by drawing para-data sets as before, but replacing individual elements of $\mathbf{s}$ with simulated data drawn from normal distributions with Σ calculated from the data for an entire site. This procedure goes a long way toward calculating realistic confidence intervals from sites with too few samples.

Speaking of "too few samples", we emphasize that bootstrapped confidence ellipses are only asymptotically correct, relying on the assumption that the full statistical variability is represented in the data set. It is inadvisable to rely on bootstrapped uncertainties with fewer than about 20 specimens as they will be too small. If it is possible to perform a parametric bootstrap (i.e., the δs are normally distributed), then perhaps as few as six samples can be done. Borradaile (2003) states incorrectly that the bootstrap is preferable for small sample sizes, this being only true if a parametric bootstrap can be performed.

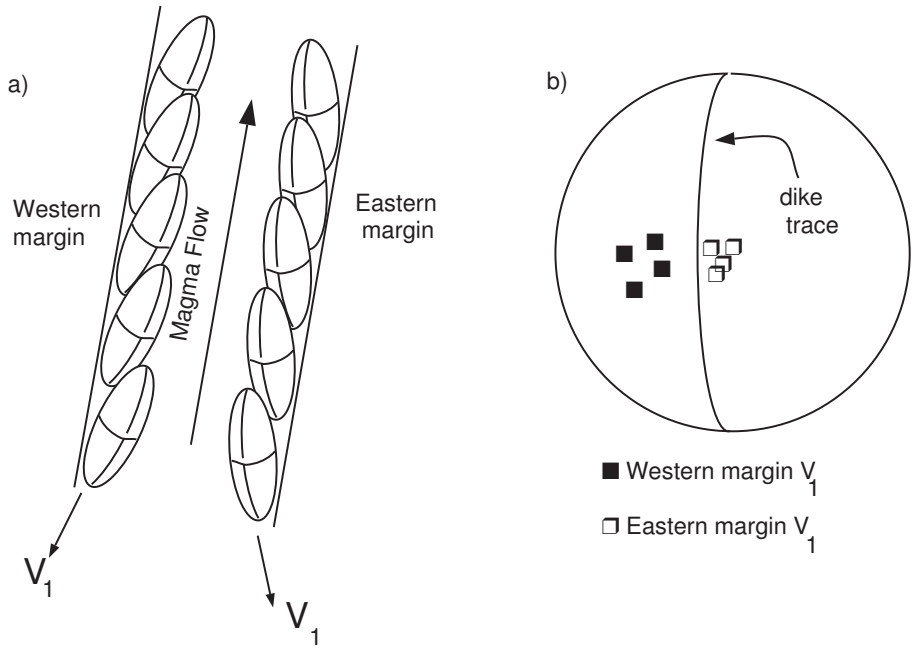

Figure 13.6: Principles of AMS for interpretation of flow directions in dikes (see Knight and Walker, 1988.)

13.8 Comparing mean eigenvectors with other axes

We can now consider whether a particular axis is distinct from a given direction or another eigenvector. For example, we may wish to know if a given data set from a series of sediments has a vertical minor eigenvector as would be expected for a primary sedimentary fabric. In Figure 13.5a we show AMS data from samples taken from the Scaglia Bianca Formation (Cretaceous white limestones) in the Umbrian Alps of Italy. They have been rotated into tilt adjusted coordinates; hence the bedding pole is vertical. Instead of plotting the 95% confidence ellipses, which all require unnecessary parametric assumptions, we show the bootstrap eigenvectors in Figure 13.5b. The smear of points certainly covers the vertical direction, consistent with a vertical direction for $\mathbf{V}_3$. To make the test at a given level of confidence (say 95%), we can employ the method developed for unit vectors in which the eigenvector of choice (here $\mathbf{V}_3$) is converted to cartesian coordinates and sorted. Then the bootstrapped 95% confidence bounds can be directly compared with the expected value. For a direction to be vertical, both the x_1 and x_2 components must be indistinguishable from zero. We plot v_{31} and v_{32} as histograms, with the 95% confidence bounds shown above in Figure 13.5. The expected value of zero is shown by dashed lines. Because zero is included within the confidence intervals, these data have a direction of $\mathbf{V}_3$ that cannot be distinguished from vertical at the 95% level of confidence.

Another question that often arises is whether eigenvectors from two sets of AMS data can be distinguished from one another. For example, are the $\mathbf{V}_1$ directions from data sets collected from two margins of a dike different from one another and on opposite sides of the dike plane as expected from anisotropy controlled by crystal imbrication.

The principles by which flow directions can be determined in volcanic dikes were laid out by

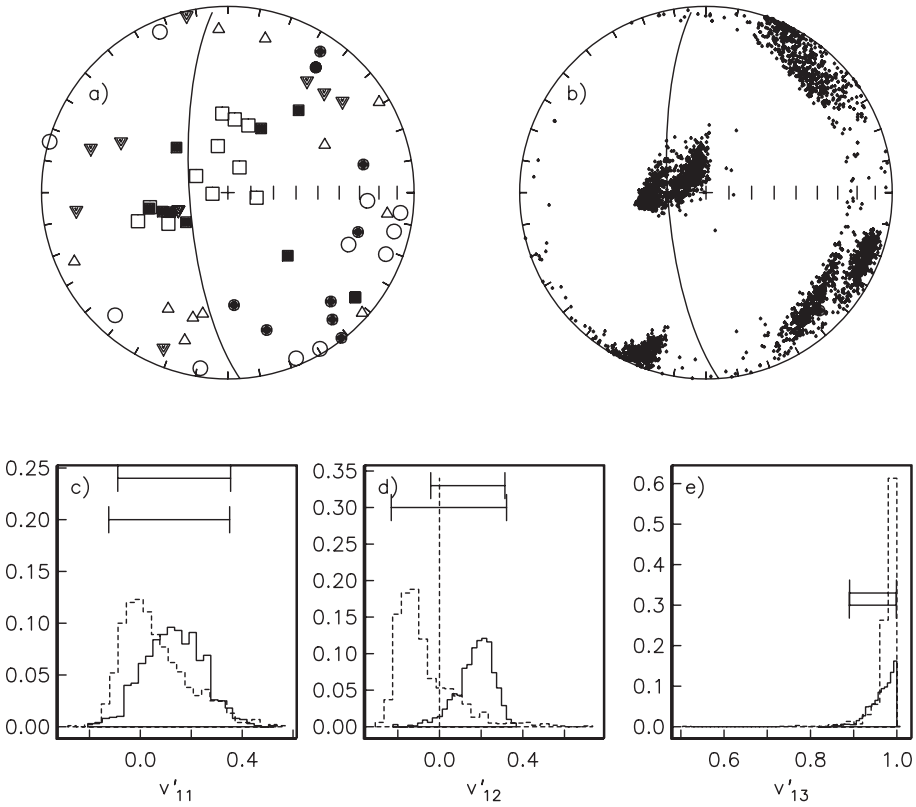

Figure 13.7: AMS data obtained from samples from the margins of a nearly vertical dike in the Troodos Ophiolite. a) Equal area projection of principal (squares), major (triangles), and minor (circles) eigenvectors. Data from the Eastern (Western) margins are shown as open (solid) symbols. The dike trace is shown as a great circle. b) Bootstrapped eigenvectors from the data shown in a). c) Histogram of cartesian coordinates v'_{11} of the bootstrapped principal eigenvectors. These have been rotated into "dike coordinates" (see text). d) Same as c) but for v'_{12}. The dike plane (dashed line) is centered with respect to the $\mathbf{X}_2$ direction. The v_{12} componenent from neither margin is distinct from the dike plane or from each other, based on the 95% confidence bounds drawn above the histograms. e) Same as c) but for v'_{13}.

Knight and Walker (1988). While the magma is flowing in the dike, elongate particles become imbricated against the chilled margins (see Figure 13.6). Opaque phases such as magnetite are often observed to be distributed along the fabric of the silicate phases (see Hargraves, 1991). The principal eigenvectors arising from such a *distribution anisotropy* parallel the fabric of the silicates. In Figure 13.6b, we show that in the ideal case, the $\mathbf{V}_1$ directions from the two margins are distinct and fall on either side of the dike trace. Because the convention is to plot AMS data in lower hemisphere projections, the fact that the western margin data plot on the western side, and the eastern margin data plot on the eastern side suggests that the flow was upward. Thus, the AMS data from chilled margins of dikes can give not only a lineation, but a well constrained direction of magma flow.

In Figure 13.7a, we show the eigenvectors of AMS data from samples obtained from both quenched margins of a nearly vertical north-south trending dike in the Troodos Ophiolite in Cyprus.

The bootstrapped eigenvectors are shown in Figure 13.7b. In order to address the problem of whether the $\mathbf{V}_1$s are distinct from the dike plane, we first rotate them into *dike coordinates* (whereby the dike pole is parallel to X_2 and direction of dip is parallel to X_3). Then the question of whether the $\mathbf{V}_1$ direction is distinct reduces to whether the v_{12} components can be distinguished from zero (the dike plane). In Figure 13.7c, we show the histogram of the cartesian components of $\mathbf{V}_1$ and the 95% confidence intervals of the two data sets. As we can see from the overlapping confidence bounds, the data are neither distinct from the dike margin, nor from each other.

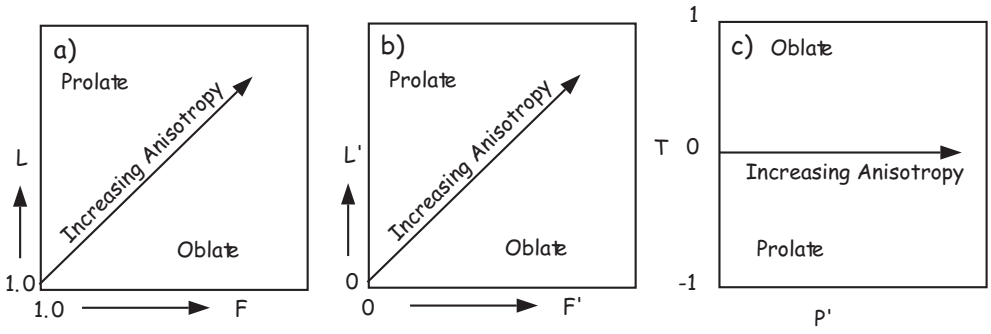

Figure 13.8: Properties of various AMS diagrams: a) Flinn, b) Ramsay and c) Jelinek.

13.9 Shape

There are innumerable ways of plotting and characterizing shapes of AMS ellipsoids in the literature. We will focus here on a few and discuss how bootstrapping could be helpful in providing a means for discriminating differences in data sets and so on. We list some popular so-called "shape parameters" in Table 14.1.

Many researchers use the "total anisotropy" parameter of Owens (1974). This has the uncomfortable property of ranging up to 300%; hence, we prefer the parameter called here the % anisotropy of Tauxe et al. (1990) as this ranges from 0 - 100%. The so-called "corrected anisotropy" of Jelinek (1981) has several definitions in the literature (compare for example Borradaile (1988) with Jelinek (1981); we have used the original definition of Jelinek (1981).

With the plethora of parameters comes a host of plotting conventions. We will consider five types of plots here: histogram of bootstrapped eigenvalues, the Flinn diagram (F versus L) after Flinn (1962], the Ramsay diagram (F' versus L') after Ramsay (1967), the Jelinek diagram (P' versus T) after Jelinek (1981), and the ternary projection (see Woodcock, 1977 and Tauxe et al., 1990). The Flinn, Ramsay, and Jelinek diagrams are shown in Figure 13.8 and the ternary projection is shown in Figure 13.10.

The Flinn and Ramsay diagrams are very similar, but the Ramsay plot has the advantage of having a zero minimum as opposed to starting at 1.0 as in the Flinn diagram. Both are essentially polar plots, with radial trajectories indicating increasing anisotropy. Shape is reflected in the angle, with "oblate" shapes above the line and "prolate" shapes below.

It is important to remember that, in fact, only points along the plot axes themselves are truly oblate or prolate and that all the area of the plot is in the "triaxial" region. Because of statistical uncertainties, samples that plot in this region may fail the F_{12} or F_{23} tests of Hext and be classifiable

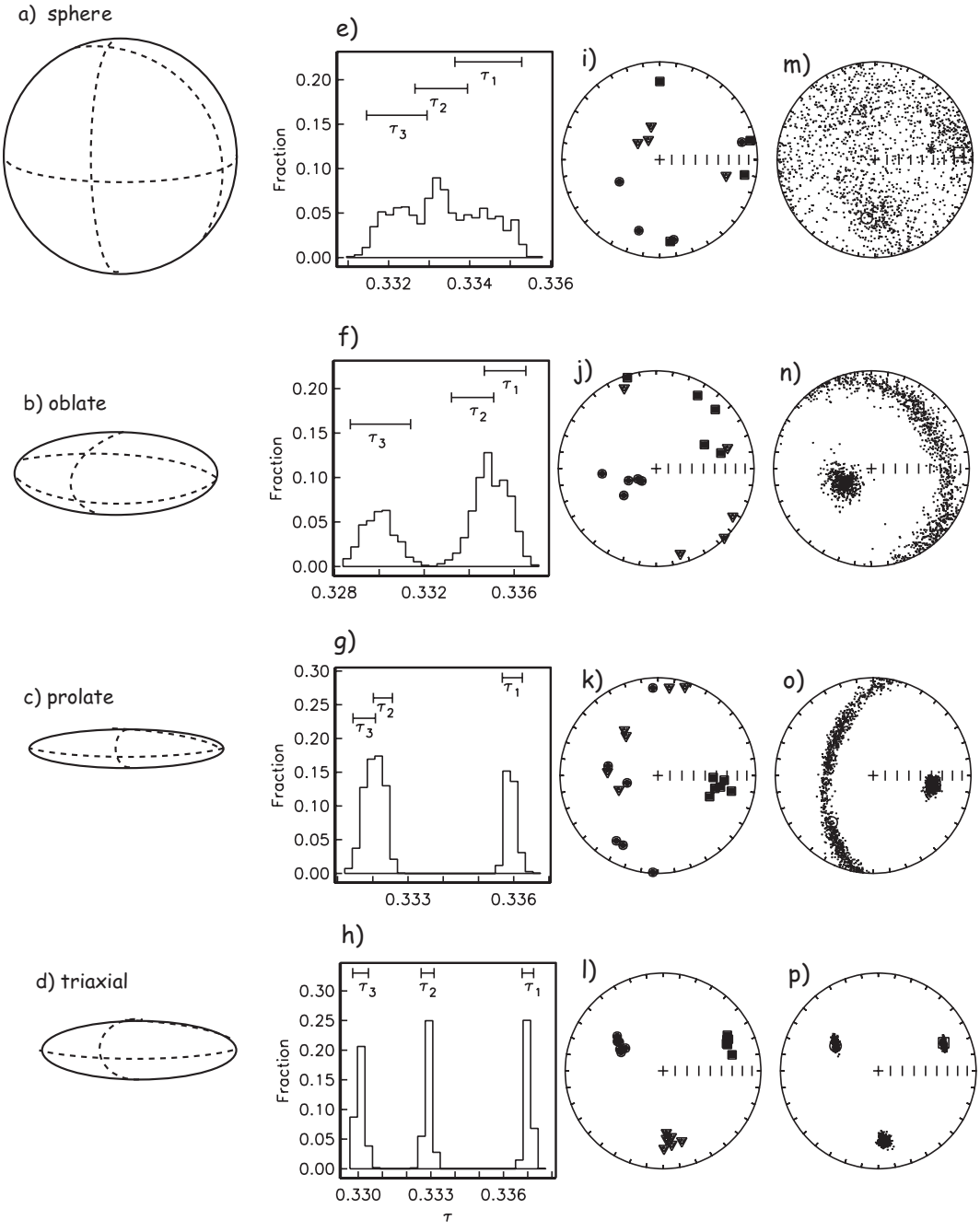

Figure 13.9: Determination shape of AMS ellipsoids using the bootstrap. a)-d) Magnitude ellipsoids. e)-h) Histograms of the bootstrapped eigenvalues associated with the eigenvectors plotted in i)-l) (same conventions as in Figure 5). The bounds containing 95% of each eigenvalue are shown above the histograms. m)-p) Bootstrapped eigenvectors.

as "oblate" or "prolate". In general, however, only a narrow zone near the axes can be considered oblate or prolate, so these terms are often used loosely.

The Jelinek diagram is more cartesian in nature than the Flinn or Ramsay plots. "Corrected" anisotropy increases along the horizontal axis and shape reflected in the vertical axis. There is no real advantage to using the highly derived P' and T parameters over the Ramsay or Flinn plots. Nonetheless they are quite popular (Tarling and Hrouda, 1993).

In the ternary projection, there are actually three axes (see Figure 13.10a). The projection can be plotted as a normal X-Y plot by using the E' and R parameters listed in Table 1 (see Figure 13.10b).

In none of the various types of plots just discussed are the horizontal and vertical axes independent of one another, but all the diagrams reflect the essence of the ellipsoid shape. Unlike the histogram with bootstrap confidence intervals, it is not possible to determine whether the various eigenvalues or ratios thereof can be distinguished from one another in a statistical sense.

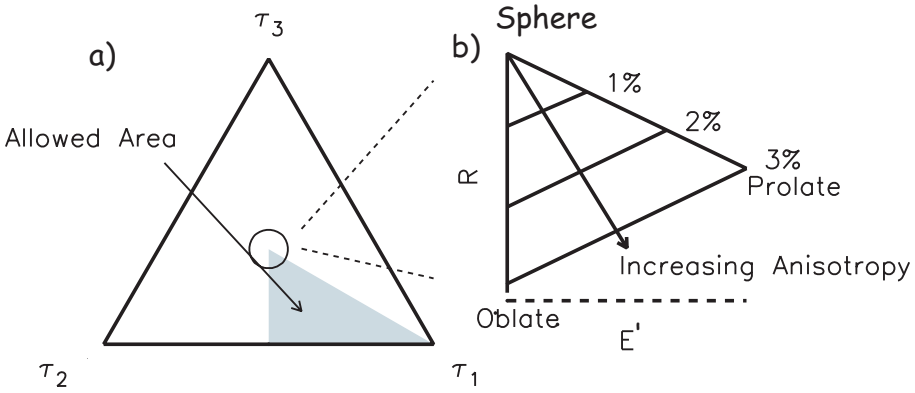

Figure 13.10: Properties of the Ternary diagram: a) there are three axes with limits of τ_1, τ_2, τ_3. Because of the constraint that $\tau_1 > \tau_2 > \tau_3$, only the shaded region is allowed. This is bounded at the top by a sphere when all three eigenvalues are equal, to the bottom left by a disk and to the bottom right by a needle. Geological materials generally have a low degree of anisotropy and plot close to the sphere. This region is enlarged in b) which illustrates how the ternary projection can be plotted as E' versus R and how shape (oblate, prolate, sphere) and percent anisotropy appear on the diagram.

All discussions of the "shape" of the AMS ellipsoid revolve around the relationships between the various eigenvalues. The first question to consider is whether these can be distinguished in a statistical sense. The Hext version of linear perturbation analysis has the ability to check for significance of the anisotropy (using the F parameters). However, the approximations involved in the Hext method make it inappropriate for most data sets involving more than one sample. Bootstrapping allows for testing the significance of the differences in eigenvalues and the less restrictive assumptions allow bootstrap tests to be applied more widely.

The simplest means of determining whether two sets of eigenvalues are distinct from one another requires the assumption that the bootstrapped eigenvalues are normally distributed. Here we calculate the standard deviations of the populations of eigenvalues. While the eigenvalues may often satisfy the requirement of normal distribution, they equally often may not. Hence, we desire a less restrictive way of deciding whether eigenvalues are distinct.

13.9. SHAPE

One alternative way of checking whether eigenvalues can be discriminated is quite similar to the bootstrap test for common mean described in Lecture 12. In Figure 13.9a-d, we sketch the four shape categories defined in the beginning of the chapter. The eigenvectors calculated for samples from four sites are shown in Figure 13.9i-l. Bootstrapped eigenvectors are shown in Figure 13.9m-p. Histograms of the associated bootstrapped eigenvalues are shown in Figure 13.9e-h. There are three "humps" in all of the histograms, but the 95% confidence bounds provide a means for quantifying the shape tests defined earlier.

In Figure 13.9a, we illustrate the behavior of data from an AMS ellipsoid that is essentially spherical in shape. The three eigenvalues plotted in the histogram (Figure 13.9e) have overlapping confidence intervals, hence they are indistinguishable. The corresponding bootstrapped eigenvectors shown in Figure 13.9m plot in a cloud with no preferred orientations.

In Figure 13.9b we show data characteristic of an oblate ellipsoid. The smallest eigenvalue is distinct from the other two in Figure 13.9f, but the 95% confidence bounds of τ_2 overlap those of τ_1. The $\mathbf{V}_3$ eigenvector is consequently reasonably well defined, but the distribution of bootstrapped $\mathbf{V}_2$ and $\mathbf{V}_1$ form a girdle distribution (Figure 13.9n).

The data from a prolate ellipsoid (see Figure 13.9c) have a distinct τ_1 distribution (Figure 13.9g), while τ_2 and τ_3 are clumped together. The $\mathbf{V}_1$ directions are nicely defined, but the $\mathbf{V}_2$ and $\mathbf{V}_3$ directions are smeared in a girdle (Figure 13.9o)).

Finally, the triaxial case is shown in Figure 13.9d. All three eigenvalues are distinct (Figure 13.9h) and the corresponding eigenvectors well grouped (Figure 13.9p).

There is no "right" way to plot eigenvalue data. Each application requires careful thought as to what is actually being tested. What do you want to know? The histogram method illustrated in Figure 13.9 is most appropriate for classifying shape characteristics of a relatively homogeneous set of samples. However, it may not be ideal for examining trends in behavior among samples or data sets. For example, one may wish to show the progressive change in shape and degree of anisotropy as a function of metamorphism. In such a case, one of the other plots (Flinn, Ramsay, Jelinek, or ternary) may serve better. Or one may wish to examine temporal trends in shape, for example the progressive change in sedimentary fabric with depth. In this case, plots of eigenvalues versus stratigraphic position may be the most useful way of looking at the data.

Table 13.1: Assorted anisotropy parameters.

Parameter (Reference)	Equation
Bulk Susceptibility (see text)	$\chi_b = (s_1 + s_2 + s_3)/3$
Normalized eigenvalues (see text)	$\tau_1 + \tau_2 + \tau_3 = 1$
Log eigenvalues (Jelinek, 1981)	$\eta_1 = \ln \tau_1; \eta_2 = \ln \tau_2; \eta_3 = \ln \tau_3$
Log mean susceptibility (Jelinek, 1981)	$\bar{\eta} = (\eta_1 + \eta_2 + \eta_3)/3$
Magnitude of Anisotropy:	
% Anisotropy (Tauxe et al. , 1990)	$\%h = 100(\tau_1 - \tau_3)$
"Total" Anisotropy (Owens, 1974)	$A = (s_1 - s_3)/\chi_b$
Anisotropy Degree (Nagata, 1961)	$P = \tau_1/\tau_3$
"Corrected" Anisotropy (Jelinek, 1981)	$P' = \exp\sqrt{2[(\eta_1 - \bar{\eta})^2 + (\eta_2 - \bar{\eta})^2 + (\eta_3 - \bar{\eta})^2]}$
Shape:	
Shape Factor (Jelinek, 1981])	$T = (2\eta_2 - \eta_1 - \eta_3)/(\eta_1 - \eta_3)$
Lineation (Balsley and Buddington, 1960)	$L = \tau_1/\tau_2$
Foliation (Stacey et al., 1960)	$F = \tau_2/\tau_3$
log Lineation (Woodcock, 1977)	$L' = \ln(L)$
log Foliation (Woodcock, 1977)	$F' = \ln(F)$
Elongation (Tauxe, 1998)	$E' = \tau_1 + .5\tau_3$
Roundness (Tauxe, 1998)	$R = \sin(60)\tau_3$

Appendix

A The 15 measurement protocol

The Jelinek (1976) 15 measurement scheme is illustrated in Figure A1. This is the procedure recommended in the manual distributed with the popular Kappabridge susceptiblity instruments. In the 15 measurement case shown in Figure A1, the design matrix is:

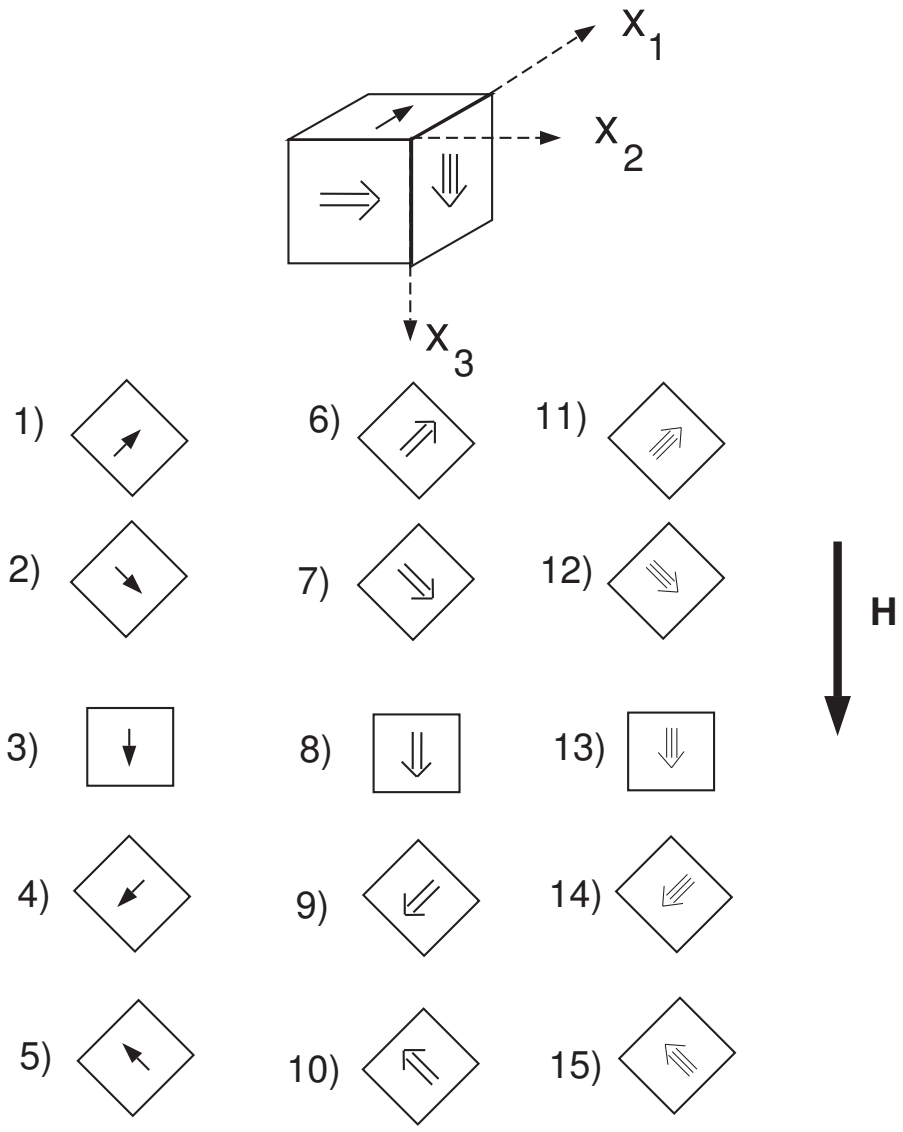

Figure A1: The 15 position scheme of Jelinek (1976) for measuring the AMS of a sample.

$$\mathbf{A} = \begin{pmatrix} .5 & .5 & 0 & -1 & 0 & 0 \\ .5 & .5 & 0 & 1 & 0 & 0 \\ 1 & 0 & 0 & 0 & 0 & 0 \\ .5 & .5 & 0 & -1 & 0 & 0 \\ .5 & .5 & 0 & 1 & 0 & 0 \\ 0 & .5 & .5 & 0 & -1 & 0 \\ 0 & .5 & .5 & 0 & 1 & 0 \\ 0 & 1 & 0 & 0 & 0 & 0 \\ 0 & .5 & .5 & 0 & -1 & 0 \\ 0 & .5 & .5 & 0 & 1 & 0 \\ .5 & 0 & .5 & 0 & 0 & -1 \\ .5 & 0 & .5 & 0 & 0 & 1 \\ 0 & 0 & 1 & 0 & 0 & 0 \\ .5 & 0 & .5 & 0 & 0 & -1 \\ .5 & 0 & .5 & 0 & 0 & 1 \end{pmatrix}, \tag{A1}$$

and $\mathbf{B} = \frac{1}{20}\times$

$$\begin{pmatrix} 3 & 3 & 8 & 3 & 3 & -2 & -2 & -2 & -2 & -2 & 3 & 3 & -2 & 3 & 3 \\ 3 & 3 & -2 & 3 & 3 & 3 & 3 & 8 & 3 & 3 & -2 & -2 & -2 & -2 & -2 \\ -2 & -2 & -2 & -2 & -2 & 3 & 3 & -2 & 3 & 3 & 3 & 3 & 8 & 3 & 3 \\ -5 & 5 & 0 & -5 & 5 & 0 & 0 & 0 & 0 & 0 & 0 & 0 & 0 & 0 & 0 \\ 0 & 0 & 0 & 0 & 0 & -5 & 5 & 0 & -5 & 5 & 0 & 0 & 0 & 0 & 0 \\ 0 & 0 & 0 & 0 & 0 & 0 & 0 & 0 & 0 & 0 & -5 & 5 & 0 & -5 & 5 \end{pmatrix}. \tag{A2}$$

B Hext confidence ellipses

The Hext (1963) confidence ellipses shown in Figure 13.3 are calculated as follows:

1. We assume that the uncertainties in the eigenvectors are in a plane that is tangent to the unit sphere. We further assume that they belong to a two-dimensional normal distribution with semi-axes that are aligned along the $\mathbf{V}_i$. The ellipse with semi-axes ϵ_{ij} that outline a 95% confidence region in this plane is then projected onto the sphere (Figure 13.3).

2. Calculate the matrices $\bar{\mathbf{s}}$, $\bar{\mathbf{K}}$, and the δ_i from the measured values of $\mathbf{K}$.

3. Calculate the eigenvectors $\mathbf{V}$ and eigenvalues τ of $\bar{\mathbf{s}}$.

4. Calculate σ by Equations 13.12 and 13.13.

5. The confidence regions are outlined by ellipses along semi-axes ϵ_{ij} aligned with the eigenvectors. The i subscripts refer to the axis on which the ellipse is attached and the j subscripts refer to the axis to which it points. Thus, ϵ_{12} is the semi-axis that defines the confidence region of $\mathbf{V}_1$ directed toward $\mathbf{V}_2$ (Figure 13.3).

   The three unique semi-angles of the confidence ellipses ϵ_{ij} are calculated by:

$$\begin{aligned} \epsilon_{12} &= \tan^{-1}[f\sigma/2(\tau_1-\tau_2)] \\ \epsilon_{23} &= \tan^{-1}[f\sigma/2(\tau_2-\tau_3)] \\ \epsilon_{13} &= \tan^{-1}[f\sigma/2(\tau_1-\tau_3)] \\ \epsilon_{21} &= \epsilon_{12} \\ \epsilon_{32} &= \epsilon_{23} \\ \epsilon_{31} &= \epsilon_{13}, \end{aligned} \tag{B1}$$

where

$$f = \sqrt{2(F_{(2,n_f);(1-p)})},$$

and where $F_{(2,n_f)}$ is the value from the F table (see Table D1 of Lecture 11), with 2 and n_f degrees of freedom, at the p probability level. The value of $F_{(2,n_f)}$ for $N_{meas} = 15$ measurements ($n_f = 9$) at the 95% level of confidence ($p = .05$) is 4.26 and so $f = 2.92$.

C Hext F statistics for significance of eigenvalue ratios

Because of the mindless precision of modern computers, there are always three different eigenvalues returned by subroutines for eigenparameter calculation. But, these may not be significantly different from one another. In order to test for significance, Hext (1963) developed three F statistics: F for significance of overall anisotropy, F_{12} for significant difference between the maximum and intermediate eigenvalues (are the data oblate?) and F_{23} for significant difference between the intermediate and minimum eigenvalues (are the data prolate?). (If all three are positive, the data are triaxial). The F statistics are calculated as follows:

$$\begin{aligned} F &= 0.4(\tau_1^2+\tau_2^2+\tau_3^2-3\chi_b^2)/\sigma^2 \\ F_{12} &= 0.5((\tau_1-\tau_2)/\sigma)^2 \\ F_{23} &= 0.5((\tau_2-\tau_3)/\sigma)^2, \end{aligned} \tag{C1}$$

where the bulk susceptibility χ_b is given by:

$$\chi_b = (\bar{s}_1+\bar{s}_2+\bar{s}_3)/3. \tag{C2}$$

The critical value for F (see F Table in the appendix to Lecture 9) is 3.4817 for 95% confidence (for F_{12} and F_{23}, it is 4.2565).

D Correction of inclination error with AARM

The magnitude of ARM is here denoted M_a. The particle anisotropy is denoted a and is defined as the and is given by:

$$a = [\frac{M_{a_{||}}}{M_{a_\perp}}]_{particle} \tag{D1}$$

where $M_{a_{||}}$ and $M_{a_\perp}$ are the magnitudes of the ARM acquired parallel to and perpendicular to the detrital particle long axis respectively. The normalized eigenvalues of the ARM tensor (q_i) are defined as:

$$q_i = \frac{M_{a_i}}{M_a}.$$

Stephenson et al. (1986) defined an orientation distribution function for the preferred alignment of particle long axes whose eigenvalues are given by κ_i where $\kappa_1 > \kappa_2 > \kappa_3$ as usual. Jackson et al. (1991) collect together the two sources of anisotropy (alignment of particle long axes and individual particle anisotropies) as:

$$\kappa_i = \frac{q_i(a+2)-1}{(a-1)}. \tag{D2}$$

Assuming that the DRM anisotropy is identical to the orientation distribution function of particle long axes we can combine and rearrange Equations 13.16 and D2 to get the relationship between the flattening factor f and the ARM anisotropy:

$$f = \frac{q_3(a+2)-1}{q_1(a+2)-1}$$

From the forgoing, measuring the AARM tensor yields the values for q, but determining values for a are more problematic. Vaughn et al. (2005) describe a technique whereby magnetic particles are separated from the matrix, then allowed to dry in an epoxy matrix in the presence of a magnetic field sufficient to fully align the long axes of the magnetic particles (say 50 mT). The AARM parallel to and perpendicular to the axis of alignment therefore gives a by Equation D1.

Bibliography

Aitken, M., Alcock, P., G.D., B. & Shaw, C. (1981), 'Archaeomagnetic determination of the past geomagnetic intensity using ancient ceramics: allowance for anisotropy', *Archaeometry* **23**, 53–64.

Balsley, J. R. & Buddington, A. F. (1960), 'Magnetic susceptibility anisotropy and fabric of some Adirondack granites and orthogneisses', *Amer. Jour. Sci.* **258A**, 6–20.

Borradaile, G. J. (1988), 'Magnetic susceptibility, petrofabrics and strain', *Tectonophysics* **156**, 1–20.

Borradaile, G. J. (2003), *Statistics of Earth Science Data: Their Distribution in Time, Space, and Orientation*, Springer, Berlin.

Collinson, D. W. (1983), 'Methods in Rock Magnetism and Paleomagnetism'.

Constable, C. & Tauxe, L. (1990), 'The bootstrap for magnetic susceptibility tensors', *J. Geophys. Res.* **95**, 8383–8395.

Flinn, D. (1962), 'On folding during three-dimensional progressive deformation', *Geol. Soc. London Quart. Jour.* **118**, 385–433.

Hargraves, R. B. (1991), 'Distribution anisotropy: the cause of AMS in igneous rocks?', *Geophys. Res. Lett.* **18**, 2193–2196.

Hext, G. R. (1963), 'The estimation of second-order tensors, with related tests and designs', *Biometrika* **50**, 353–357.

Jackson, M. J., Banerjee, S. K., Marvin, J. A., Lu, R. & Gruber, W. (1991), 'Detrital remanence, inclination errors and anhysteretic remanence anisotropy: quantitative model and experimental results', *Geophys. J. Int.* **104**, 95–103.

Jelinek, V. (1976), 'The statistical theory of measuring anisotropy of magnetic susceptibility ofrocks and its application', *unpublished.* .

Jelinek, V. (1978), 'Statistical processing of anisotropy of magnetic susceptibility measured on groups of specimens', *Studia Geophys. et geol.* **22**, 50–62.

Jelinek, V. (1981), 'Characterization to the magnetic fabric of rocks', *Tectonophys.* **79**, 63–67.

King, R. F. (1955), 'The remanent magnetism of artificially deposited sediments', *Mon. Nat. Roy. astr. Soc., Geophys. Suppl.* **7**, 115–134.

Knight, M. D. & Walker, G. P. L. (1988), 'Magma flow directions in dikes ofteh Koolau Comples, Oahu, determined from magnetic fabric studies', *Jour. Geophys. Res.* **93**, 4301–4319.

Levi, S. & Banerjee, S. K. (1976), 'On the possibility of obtaining relative paleointensities fromlake sediments', *Earth Planet. Sci. Lett.* **29**, 219–226.

Means, W. (1976), *Stress and Strain: Basic Concepts of Continuum Mechanics for Geologists*, Springer-Verlag.

Nagata, T. (1961), 'Rock Magnetism'.

Nye, J. F. (1957), 'Physical Properties of Crystals'.

Owens, W. H. (1974), 'Mathematical model studies on factors affecting the magnetic anisotropy of deformed rocks', *Tectonophys.* **24**, 115–131.

Ramsay, J. G. (1967), 'Folding and fracturing of rocks'.

Stacey, F. D., Joplin, G. & Lindsay, J. (1960), 'Magnetic anisotropy and fabric of some foliated rocks from S.E. Australia', *Geophysica Pura Appl.* **47**, 30–40.

Stephenson, A., Sadikern, S. & Potter, D. K. (1986), 'A theoretical and experimental comparison of the susceptibility and remanence in rocks and minerals', *Geophys. J. R. astr. Soc.* **84**, 185–200.

Tarling, D. H. & Hrouda, F. (1993), 'The Magnetic Anisotropy of Rocks'.

Tauxe, L. (1998), *Paleomagnetic Principles and Practice*, Kluwer Academic Publishers, Dordrecht.

Tauxe, L., Constable, C. G., Stokking, L. B. & Badgley, C. (1990), 'The use of anisotropy to determine the origin of characteristic remanence in the Siwalik red beds of northern Pakistan', *Jour. Geophys. Res.* **95**, 4391–4404.

Vaughn, J., Kodama, K. P. & Smith, D. (2005), 'Correction of inclination shallowing and its tectonic implications: The Cretaceous Perforada Formation, Baja California', *Earth Planet. Sci. Lett.* **232**, 72–82.

Woodcock, N. H. (1977), 'Specification of fabric shapes using an eigenvalue method', *Geol. Soc. Amer. Bull.* **88**, 1231–1236.